JACS Au
AN OPEN ACCESS JOURNAL OF THE AMERICAN CHEMICAL SOCIETY

Open Access
This article is licensed under CC-BY-NC-ND 4.0

pubs.acs.org/jacsau
Article

Electrochemical Synthesis of Zeolite Coatings with Controlled Crystal Polymorphism and Self-Regulating Growth

Akash Warty, Amy Chen, Dat T. Tran, Harrison Kraus, Taylor J. Woehl, and Dongxia Liu*

Cite This: JACS Au 2024, 4, 4769–4779

Read Online

ACCESS | Metrics & More | Article Recommendations | Supporting Information

ABSTRACT: Zeolite coatings are studied as molecular sieves for membrane separation, membrane reactors, and chemical sensor applications. They are also studied as anticorrosive films for metals and alloys, antimicrobial and hydrophobic films for heating, ventilation, and air conditioning, and dielectrics for semiconductor applications. Zeolite coatings are synthesized by hydrothermal, ionothermal, and dry-gel conversion approaches, which require high process temperatures and lengthy times (ranging from hours to days). Here, we report the first zeolite coatings synthesized via electrochemical deposition on a cathodic electrode, with controlled crystal polymorphism achieved within subhourly duration. We demonstrate this approach by developing sodium zeolite (e.g., sodalite (SOD), NaA (LTA), and Linde Type N (LTN)) coatings on a titanium electrode and extending the synthesis method to porous stainless steel. The coating morphology and crystallinity depend on the temperature, time, and applied current. The coating thickness is independent of the applied current, showing the presence of a self-regulating mechanism to ensure a uniform coating thickness across the metal surface. The electrochemical zeolite growth mechanism was elucidated with high-resolution transmission electron microscopy, and applications of the resultant zeolite coatings for oil/water separation and ethanol/water pervaporation were exploited. Electrochemical synthesis represents a novel, simple, fast, and environmentally friendly approach to preparing zeolite coatings. It can potentially be generalized for developing zeolite materials with diverse framework structures, morphologies, and orientations for substrates with complicated geometries.

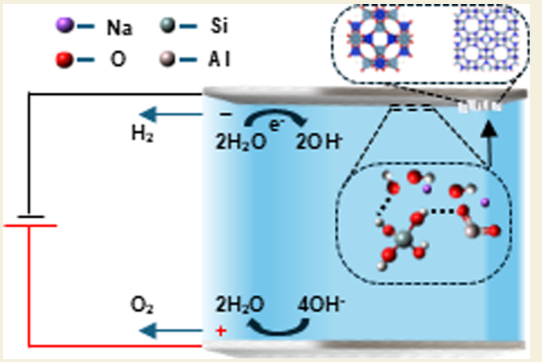

KEYWORDS: *electrochemical deposition, zeolite crystallization, crystal polymorphism, sodium zeolite, zeolite coating*

INTRODUCTION

Zeolites are crystalline microporous aluminosilicates with multifunctional properties including molecular sieving and adsorption enabled by nanometer scale cavities, ion exchange with cation sites within the negatively charged framework, hydrophilicity/hydrophobicity, and dielectric properties regulated by composition (i.e., silicon-to-aluminum (Si/Al) ratio), intrinsic nontoxicity, and thermo-chemical stability. The development of zeolite coatings with one or more of these functional properties on supportive substrates has been actively pursued for various applications. Zeolite films are well known as molecular sieves for membrane separation,[1−7] membrane reactor,[8−14] and chemical sensor applications.[15−18] Corrosion-resistant zeolite coatings have been developed for metals or alloys in severe conditions to replace chromate-based environmentally unfriendly materials.[19] The combination of hydrophilicity, adsorption, and heat transfer properties in low-silica zeolite coatings is used for HVAC (i.e., heating, ventilation, and air conditioning) systems. Films of siliceous zeolites with low dielectric constants are used for insulating media in microelectronics.[20] Antimicrobial zeolite coatings with hosted extra metal ions or particles (e.g., silver) are used for food industry or biomedical device applications.[21−23]

Different synthesis techniques have been developed for depositing zeolite coatings on substrates to impart functionalities to the components on which it is deposited. In situ crystallization was the most widely researched method in the past two decades because it allows the direct growth of zeolite crystals on the support, which offers high adhesion and cohesion between the zeolite coating and the underneath support.[24] Hydrothermal crystallization, ionothermal crystallization, and dry-gel conversion are the methods commonly applied for in situ crystallization of zeolite coatings.[24] The hydrothermal zeolite crystallization is often carried out by reacting alkaline silicate and aluminate solutions or suspensions of colloidal silica with amorphous aluminum hydroxide in alkaline solutions at a set temperature and autogenic pressure in a sealed autoclave.[2,24,25] Ionothermal crystallization uses similar reagents and conditions to those of the hydrothermal

Received: August 1, 2024
Revised: November 1, 2024
Accepted: November 4, 2024
Published: December 10, 2024

© 2024 The Authors. Published by American Chemical Society

process, except that the water solvent is replaced by ionic liquid.[19,20] An ionic liquid is a compound consisting of only ions and typically has a higher boiling temperature and lower vapor pressure than water, enabling the whole zeolite crystallization process to occur at atmospheric pressure. Different from the hydrothermal and ionothermal synthesis approaches, the dry-gel synthesis method involves crystallization of a precoated dry gel on the support into the zeolite layer in the presence of a steam environment.[26,27] Although these synthesis techniques have achieved great success in developing zeolite coatings on different substrates, all of the processes require high temperature conditions and long reaction periods (e.g., hours or days), resulting in a high energy and time cost.

Zeolite by itself does not have electronic conductivity due to the presence of a wide electronic band gap.[28] In the hydrated state, they are ionically conductive with the nature of the cation affecting the thermal activation energy of specific conductivity in zeolites with Na^+ ions exhibiting the highest conductivities.[28,29] The synthesis of zeolite, however, involves an assembly of silica and alumina around positively charged template molecules, catalyzed by negatively charged hydroxides.[30] This suggests that the application of an electric field in zeolite synthetic solution could influence the Coulomb interactions to achieve electrokinetic control of zeolite crystallization. Studies on the properties of the zeolite synthesis gel mixtures show that there is a potential gradient present between electrodes immersed in the gel.[31] The potential gradients are mainly influenced by the composition of the gel mixtures.[31] Some studies have reported the effectiveness of electrophoresis for deposition of zeolite seeds or growth of zeolite film during hydrothermal synthesis.[32,33] The application of an electric potential across the synthesis solution resulted in the deposition of zeolites on nonporous metal or secondary alumina supports where the negatively charged particles migrate toward the positively charged anode surface.[32,33] Another study developed AEL molecular sieves on the cathode by applying an electric field that resulted in the conversion of the surface of aluminum substrate to a molecular sieve in the presence of positively charged [emim]+ cations that act as structure directing agents.[34] Recently, two studies demonstrated heteroatom incorporation in hydrothermal zeolite synthesis through controlled, in situ anodic metal release.[35,36] This electro-made zeolite has a much higher framework Lewis acid site density for stannosilicates compared to batch controls.[35,36]

Herein, we report the first electrochemical deposition on a cathodic electrode to develop zeolite coatings onto a metal substrate. We demonstrate the electrochemical zeolite film synthesis approach by developing sodium zeolite (e.g., sodalite (SOD), NaA (LTA), and Linde Type N (LTN)) coatings on titanium substrates in an electrochemical cell where platinum and titanium were used as the anode and cathode electrode, respectively. The dependence of the morphology and crystallinity of zeolite coatings on synthesis temperature, time, and applied current was explored by varying these synthesis parameters. The extension of the electrochemical zeolite coating onto a porous stainless-steel substrate was explored. The as-developed zeolite coatings were characterized, and the potential growth mechanism was discussed. The applications of the resultant zeolite coatings for oil/water separation and ethanol/water pervaporation were explored. The electrochemical synthesis method is novel, simple, fast, and environmentally benign to prepare versatile zeolite coatings. We anticipate that the method can be generalized for synthesizing zeolites with diverse framework structures, morphologies, or orientation for diverse substrates with complicated geometries.

METHODS

Electrochemical Synthesis of Zeolite Coatings

A zeolite synthesis gel with a molar composition of 5 SiO_2/1 Al_2O_3/50 Na_2O/1000 H_2O was used for the electrochemical synthesis of zeolite coatings. It was prepared by dissolving required amounts of sodium hydroxide and sodium aluminate in deionized (DI) water followed by the addition of LUDOX Silica (30 wt % in water) and mixing overnight in a plastic container. A platinum plate anode and titanium or porous stainless-steel pellet was used as the cathode. Both electrodes were arranged parallel and held apart in a zeolite precursor gel solution. After the synthesis gel was heated to the desired temperature in an oil bath, the electrochemical reaction was carried out at this temperature with a constant direct current for the desired time. In the sampling experiment, a gold grid was placed on the surface of the cathode titanium electrode. After the deposition, the cathode electrode was taken out of the solution, rinsed with DI water, and dried in a convection oven. Experimental details are included in Section S1.2 of the Supporting Information file.

Material Characterizations

The crystal structures of electrochemically synthesized zeolite films were determined by powder X-ray diffraction (XRD) on a Bruker D8 diffractometer by using Cu−Kα radiation. Images of film morphology were investigated by scanning electron microscopy (SEM; Zeiss Auriga 60 CrossBeam). Focused ion beam (FIB) milling and energy-dispersive X-ray spectroscopy (EDS) were used to probe the atomic composition of the zeolite film along the sample cross-section. Scanning transmission electron microscopy EDS (STEM-EDS) and TEM/electron diffraction were performed using a JEOL JEM-ARM200F TEM microscope with a 200 kV accelerating voltage, 50 μm condenser aperture, and spot size 8C (for STEM, STEM-EDS). Contact angle of a water droplet was measured using a VCA Optima Contact Angle setup. Details can be found in Sections S1.3, S1.4, and S1.8 of the Supporting Information file.

Oil−Water Separation Measurement

A mixture of toluene and water (50/50 vol %) was used as the feed in the oil/water separation measurement. Toluene was dyed with Oil Red O dye for visibility of the different phases. The porous stainless steel or zeolite-coated porous stainless-steel membrane was attached to the bottom of a conical tube. After the toluene/water was loaded into the conical tube, vacuum was applied to the other side to provide a pressure gradient for the separation. After no further separation was observed, the volume of the permeate was measured and the oil concentration was analyzed using a UV−vis spectrophotometer to evaluate the flux and separation factor. Section S1.5 of the Supporting Information file shows the experimental details.

Ethanol/Water Pervaporation Measurement

A mixture of ethanol and water (90% ethanol/10% water, weight basis) was used at the feed for the pervaporation measurements. The coated pellet was attached to the end of a 1/4 in. stainless steel tube using epoxy and was placed in the ethanol−water mixture. The setup was then transferred to an oven preheated to the required temperature. A vacuum was applied for 30 min to the permeate side, and the permeate was collected in a cold trap using liquid nitrogen. The permeate was weighed to calculate the flux and then analyzed using gas chromatography to evaluate the separation factor. The detailed procedure can be found in Sections S1.6 and S1.7 of the Supporting Information file.

https://doi.org/10.1021/jacsau.4c00691
JACS Au 2024, 4, 4769−4779

RESULTS AND DISCUSSION

Electrochemical Synthesis of Zeolite Coating on the Titanium Substrate

The zeolite coating on a titanium cathode substrate was synthesized using a clear precursor solution with a molar composition of 5 SiO_2/1 Al_2O_3/50 Na_2O/1000 H_2O at a temperature of 333 K, ambient pressure, and galvanostatic conditions with a 1.00 A direct current. SEM images of the substrates before and after the electrochemical deposition revealed the deposition of zeolite films (Figure 1). The as-polished titanium cathode has a plain surface with some dents and roughness (Figure 1a). After electrochemical deposition for 45 min, a layer of zeolite formed on the titanium substrate containing a mix of pyramidal and cubical particles with sizes of ∼1 μm (Figure 1b). The titanium substrate is not completely covered by the deposited materials. In the spaces between these observed particles, small spherical particles (∼0.1 μm) are present. The deposition film exhibits weak crystallinity, and the phases were identified as a mixture of LTA and FAU (Figure 1d). When the synthesis time was increased to 120 min, the coverage of the particles on the film improved with intergrown particles (Figure 1c). In particular, the particles evolved to form a continuous film, with cubical particles on the film surface (∼1.5 μm) exhibiting well-defined edges interspersed with cuboctahedral particles (∼1.6 μm) with rounded edges, signaling the emergence of the LTN phase (Figure 1d). The cross-sectional view of the deposition after 120 min revealed a film thickness of ∼1.9 μm (Figure 2a). The cross-section EDS line scans (Figure 2b) showed a high Ti signal intensity from the titanium substrate, followed by an obvious drop coinciding with increase in the signal intensities of oxygen, sodium, silicon, and aluminum, which marks the beginning of the deposited zeolite coating layer on the substrate. The oxygen signal rises earlier than the those of the other three elements (e.g., between 0.8 and 1.2 μm), which suggests that an oxide layer could exist on the titanium electrode surface. The sodium signal intensity stays higher before 1.7 μm and lower after 1.7 μm than those of silicon and aluminum signals. This hints that sodium is rich in the region near the electrode surface, further confirmed by the EDS spectrum at the zeolite−metal interface (Figure S5). Minimum deposition is observed on the titanium substrate in the absence of current after 120 min (Figure S6), suggesting that zeolite crystallization on the substrate is enabled by the electrochemical deposition process. Under these synthesis conditions, zeolite growth does not take place in the bulk phase, as evidenced by the clear zeolite synthesis solution and the absence of zeolite particles collected by centrifugation at 10,000 rpm.

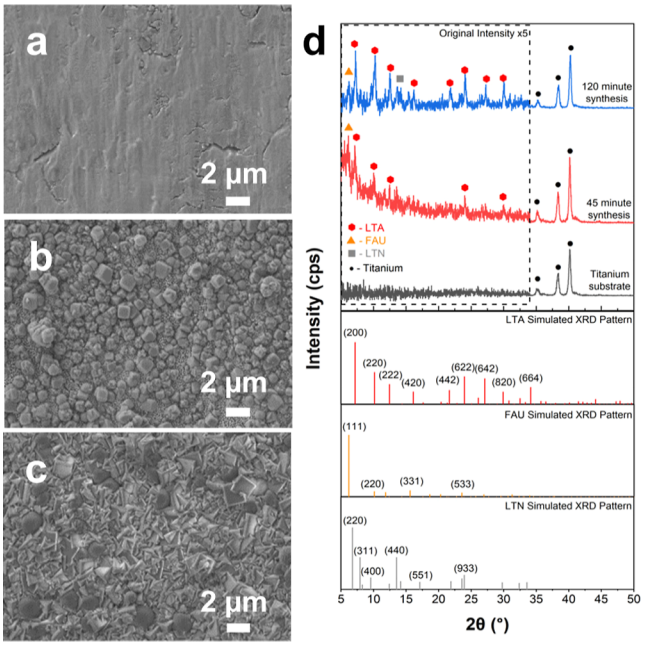

Figure 1. SEM images of titanium substrate (a) and zeolite coatings after 45 min (b) and 120 min (c) of electrochemical synthesis. (d) shows XRD patterns of the zeolite film coatings in comparison to the XRD pattern of standard LTA, FAU, and LTN zeolites (synthesis conditions: Pt anode, Ti cathode, 1.00 A direct current, 333 K, ambient pressure, 200 rpm stirring).

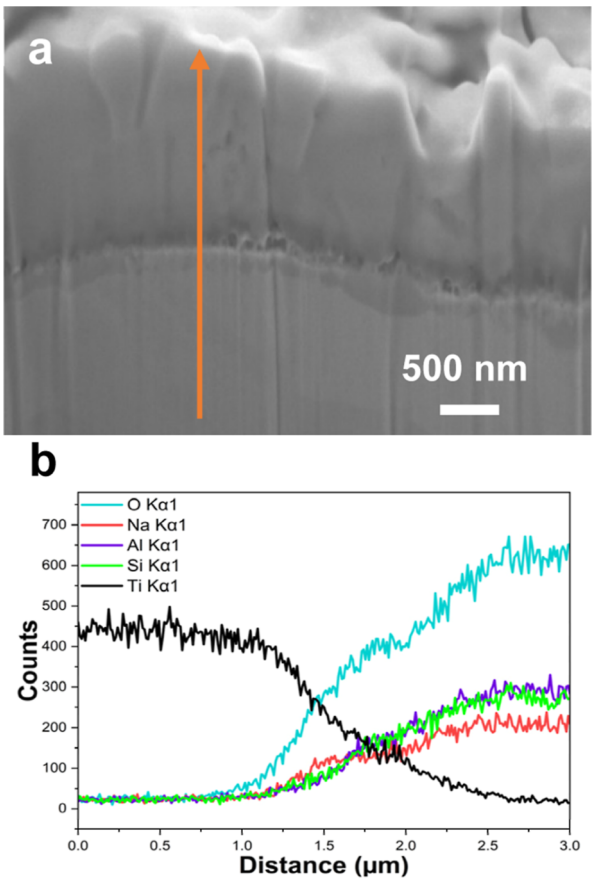

Figure 2. Cross-sectional view SEM image of zeolite coatings after 120 min after FIB milling and (b) is the EDX line scan along the orange line in (a) (synthesis conditions: Pt anode, Ti cathode, 1.00 A direct current, 333 K, ambient pressure, 200 rpm stirring).

Zeolite-Coating Polymorphism Varied by Electrochemical Deposition Conditions

The development of zeolite coatings with crystal polymorphism variation on a titanium substrate was investigated at variable synthesis conditions. The effects of electric field were studied first by varying the applied current (Figure 3a−c), in which the experimental conditions (i.e., 333 K, ambient pressure, 200 rpm magnetic stirring, 1.00 A constant current, and deposition time of 120 min) for zeolite coating in Figure 1c were used as the base case for comparison. At a low current

https://doi.org/10.1021/jacsau.4c00691
JACS Au 2024, 4, 4769−4779

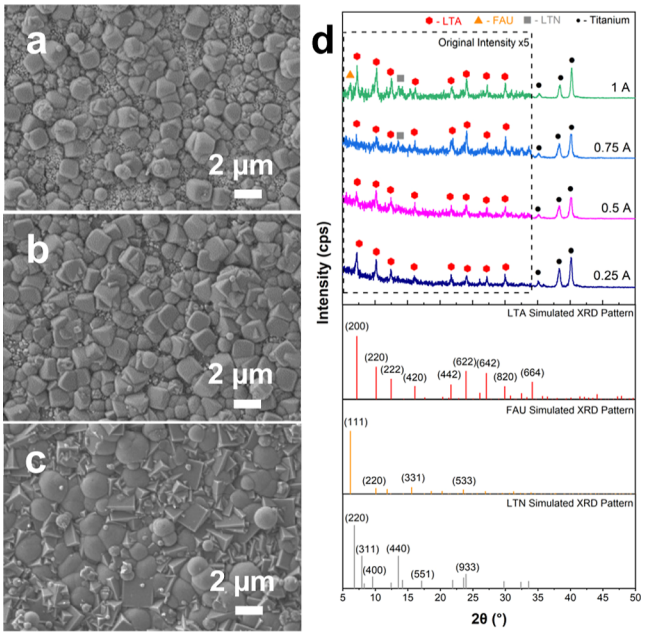

Figure 3. SEM images of zeolite coatings developed at varying current of (a) 0.25 A, (b) 0.50 A, and (c) 0.75 A at 333 K and 120 min synthesis time. (d) shows the XRD patterns corresponding to the developed zeolite contains in (a−c) in comparison with the standard XRD patterns for LTA, FAU, and LTN zeolites (synthesis conditions: Pt anode, Ti cathode, ambient pressure, 200 rpm stirring).

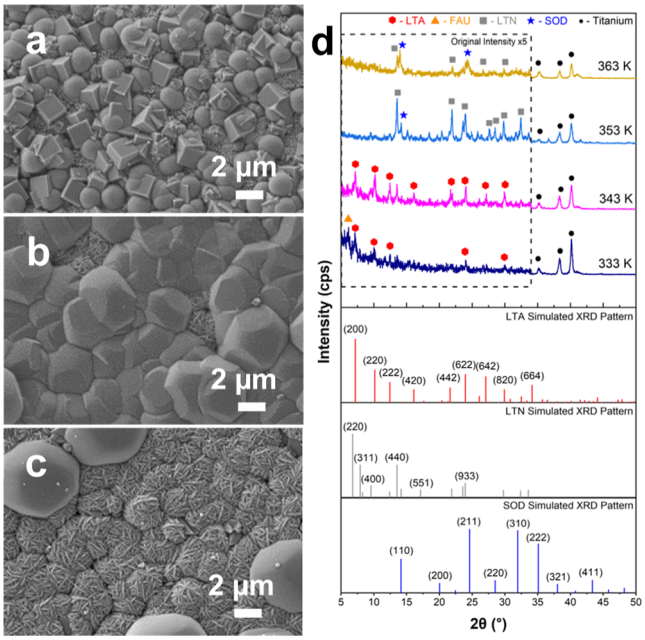

Figure 4. SEM images of zeolite coatings developed varying temperatures of (a) 343 K, (b) 353 K, and (c) 363 K at 1.00 A current and 45 min deposition time. (d) shows the XRD patterns corresponding to the developed zeolite coatings in (a−c) in comparison with the standard XRD patterns for LTA, LTN, and SOD zeolites (synthesis conditions: Pt anode, Ti cathode, ambient pressure, 200 rpm stirring).

of 0.25 A, the deposition predominantly consisted of cubic particles measuring 1.0−1.5 μm, with small (∼0.1 μm) particles filling the interparticle spaces (Figure 3a). Increasing the applied current to 0.50 A (Figure 3b) resulted in the growth of cubic particles (∼1.3 μm) with an improved surface coverage. The cubical particles have shaper edges than those synthesized at 0.25 A. Moreover, the small (∼0.1 μm) spherical particles transformed into cuboctahedron LTN particles ranging in size from 0.4 to 1.2 μm. Further elevation of the current to 0.75 A led to the formation of cubical crystals sized between 1.7 and 2.3 μm, along with large cuboctahedral particles (∼2.4 μm) with rounded edges (Figure 3c). Concurrently with the changes in morphology, the crystalline phases (Figure 3d) exhibited the LTA polymorph at 0.25 and 0.50 A and a blend of dominant LTA with a small amount of LTN at 0.75 A. Increasing the current to 1.00 A (Figure 1c) resulted in further growth of cubical particles with well-defined edges interspersed with cuboctahedral particles with rounded edges, as discussed above. Variation in applied currents induced alterations in film morphologies and crystalline phases, accompanied by improved crystallization kinetics at higher currents, leading to more complete surface coatings on the substrate.

The influence of synthesis temperature on electrochemically deposited zeolite coatings was studied by setting the synthesis gel temperature to 343, 353, and 363 K (Figure 4a−c), respectively. These tests were performed with a constant current for 45 min, using the zeolite coating in Figure 1b as the reference (i.e., ambient pressure, 200 rpm magnetic stirring, 1.00 A current, and deposition time of 45 min). Elevating the synthesis temperature from 333 (Figure 1b) to 343 K (Figure 4a) resulted in the growth of cubic LTA particles with well-defined edges, reaching sizes of ∼1.5 μm. The number of pyramidal particles and small spherical particles that were present in interstitial spaces among larger particles decreased significantly compared to observations at 333 K. The deposited layer consisted predominately of the LTA zeolite with a small amount of the LTN phase (Figure 4d). Further increasing the temperature to 353 K (Figure 4b) demonstrated nearly complete coverage of the surface by LTN particles (cuboctahedra with truncated edges) ranging from ∼3.0 to ∼5.0 μm, with thread ball-like structures (SOD) forming between them. XRD patterns (Figure 4d) confirmed the presence of LTN along with SOD crystalline phases. Finally, at 363 K, the zeolite coatings developed into spherical thread ball-like particles (SOD phase), predominantly covering the surface interspersed with cuboctahedron LTN particles (Figure 4c). The dominant crystalline phase was the SOD zeolite (Figure 4d). Overall, these results indicate that higher temperatures promote rapid electrochemical deposition kinetics, leading to growth of large particles and transformation of the zeolite crystalline phase from LTA to LTN and SOD polymorphs. For shorter times of 45 min, a continuous film was obtained only at higher temperatures of 353 K (Figure 4b) and 363 K (Figure 4c). The film thicknesses were 1.1 and 1.8 μm, respectively, evidencing faster growth kinetics at higher temperature condition.

To study effects of both electric current and temperature on morphologies of zeolite coatings, the synthesis of zeolite coating at 363 K (Figure 4c) was further explored by varying the current to 0.25, 0.50, and 0.75 A, respectively. At a low current (0.25 A), deposition primarily consisted of intertwined needle-like particles with larger particles (∼3.8 μm) buried underneath (Figure 5a). The crystalline phase is dominated by LTN along with some SOD zeolites (Figure 5d). Increasing the current to 0.50 A (Figure 5b) resulted in the formation of large truncated octahedral particles (∼4.2 μm). The needle-

https://doi.org/10.1021/jacsau.4c00691
JACS Au 2024, 4, 4769−4779

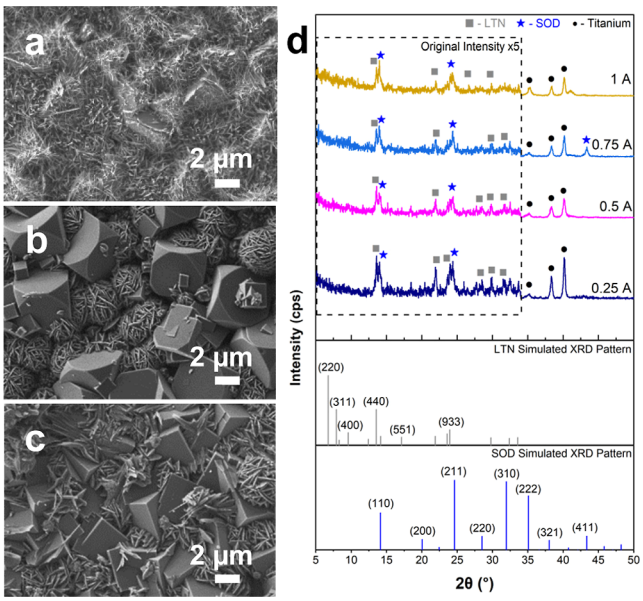

Figure 5. SEM images of zeolite coatings developed at varying current of (a) 0.25 A, (b) 0.50 A, and (c) 0.75 A at 363 K and 45 min deposition time, respectively. (d) shows the XRD patterns corresponding to the developed zeolite coatings in (a–c) in comparison with the standard XRD patterns for LTN and SOD zeolites (synthesis conditions: Pt anode, Ti cathode, ambient pressure, 200 rpm stirring).

like structures observed in Figure 5a seemed to transform into thread ball-like particles, filling the spaces among the large truncated octahedral particles. Additionally, a small number of cubical particles (~1.2 μm in size) was observed on the octahedron particles. The dominant crystalline phase still consisted of LTN mixed with a small amount of the SOD zeolite (Figure 5d). Further increase in current to 0.75 A led to the formation of a mixture of plate-like and pyramidal particles (Figure 5c). These plate particles appeared thicker and wider compared to the features grown in the thread ball-like particles observed in previous conditions. Although changes in the morphology were observed, the deposited phase exhibited crystallized LTN and SOD peaks. The coating film thicknesses were about 1.8 μm in Figure 5a–c, which seems to be independent of varied current. The effects of varying synthesis conditions are outlined in Table S1.

Sodium zeolite has often been studied as an exemplary case for zeolite structural transformation during zeolite crystallization.[37−41] Various synthesis parameters, such as the precursor composition, temperature, and time, can significantly influence polymorphism. For example, increasing temperature and/or synthesis time often initiates structural transformation stages, progressing from amorphous to crystalline and from low to high density zeolite frameworks.[37] Among sodium zeolites, LTA and FAU zeolites exhibit lower density frameworks compared to LTN and SOD zeolites,[37] which typically form under initial synthesis stage or lower temperature conditions, while the latter zeolites tend to form at a later stage or under higher temperature conditions. The present study introduces electric current as an additional parameter for tailoring structural transformations in zeolite crystallization. Similar to the effects of temperature or synthesis time, an increase in current yields effects on zeolite polymorphism comparable to those observed at higher temperatures or with prolonged synthesis times, following the Ostwald rule of stages.[37,42]

The thickness of continuous zeolite film coatings does not seem to increase proportionally with increasing current, in contrast to the relationship observed with increasing temperature or synthesis time.[37] This discrepancy likely arises from the growing heterogeneity of the electric field magnitude on the cathode, as the surface becomes increasingly covered by zeolite. During the deposition process, regions of the cathode surface covered by zeolite are likely to experience a weaker electric field compared to adjacent regions that remain free of zeolite coverage. This disparity is conducive to enhanced zeolite nucleation and growth in the uncovered regions, while growth in regions already covered by zeolite is slowed. Consequently, lateral growth predominates on the cathode surface over in-depth growth. Once the cathode surface is entirely coated by zeolite, the electric field weakens between the electrodes, leading to a deceleration in zeolite growth across the entire surface. This self-regulating growth mechanism facilitates the development of zeolite coatings with a uniform thickness across the cathode substrate. This contrasts with Ostwald ripening of particles under high temperature, which grows large crystals at the expense of smaller ones during zeolite synthesis, leading to inhomogeneous particle size.[42] The electrochemical synthesis of zeolite coatings presents a novel self-regulating mechanism for achieving uniform coatings on the substrates.

Electrochemical Zeolite Growth Mechanism

The synthesis of zeolite involves the assembly of negatively charged tetrahedrally coordinated silicon and aluminum species around positively charged template molecules catalyzed by negatively charged hydroxides. The influence of an electric field on zeolite synthesis may stem from multiple mechanisms, including electrophoresis, in situ water splitting, and electrochemical deposition of silicate and aluminate species from the zeolite precursor gels. Electrophoresis typically results in zeolite deposition on the positively charged anode. This mechanism has been explored for coating zeolite seeds on a charged support for secondary hydrothermal synthesis[32,33] or driving zeolite particles to the anode support for membrane zeolite preparation.[43,44] It should be noted that electrophoretic deposition of hydrothermally synthesized zeolite particles often requires hours to complete due to the constrained zeolite formation rate during hydrothermal growth. Our study observed rapid (e.g., subhourly) zeolite growth on the cathode, suggesting that electrophoresis of the silicate and aluminate anions, driven by the potential gradient between the metal electrodes, should not be the mechanism in the electrochemical synthesis of zeolite coatings. Besides, no zeolite coatings were observed on the Pt anode under all tested electrochemical deposition conditions.

In situ water electrolysis occurred in the electrochemical synthesis of zeolite coatings, as evidenced by the evolution of gas bubbles on both electrode surfaces. At the negatively charged cathode, water reduction occurs, leading to evolution of hydrogen gas and an increase in pH (see eq 1 in Figure 6a). This local pH increase can facilitate the electrochemical deposition of inorganic coating materials, as reported for electrochemical synthesis of hydroxyapatite[45−47] and silicate[48] materials. Zeolite crystallization requires a basic condition, so pH plays a crucial role in influencing its nucleation and growth.[49] We anticipate that the high negative potential of the

https://doi.org/10.1021/jacsau.4c00691
JACS Au 2024, 4, 4769−4779

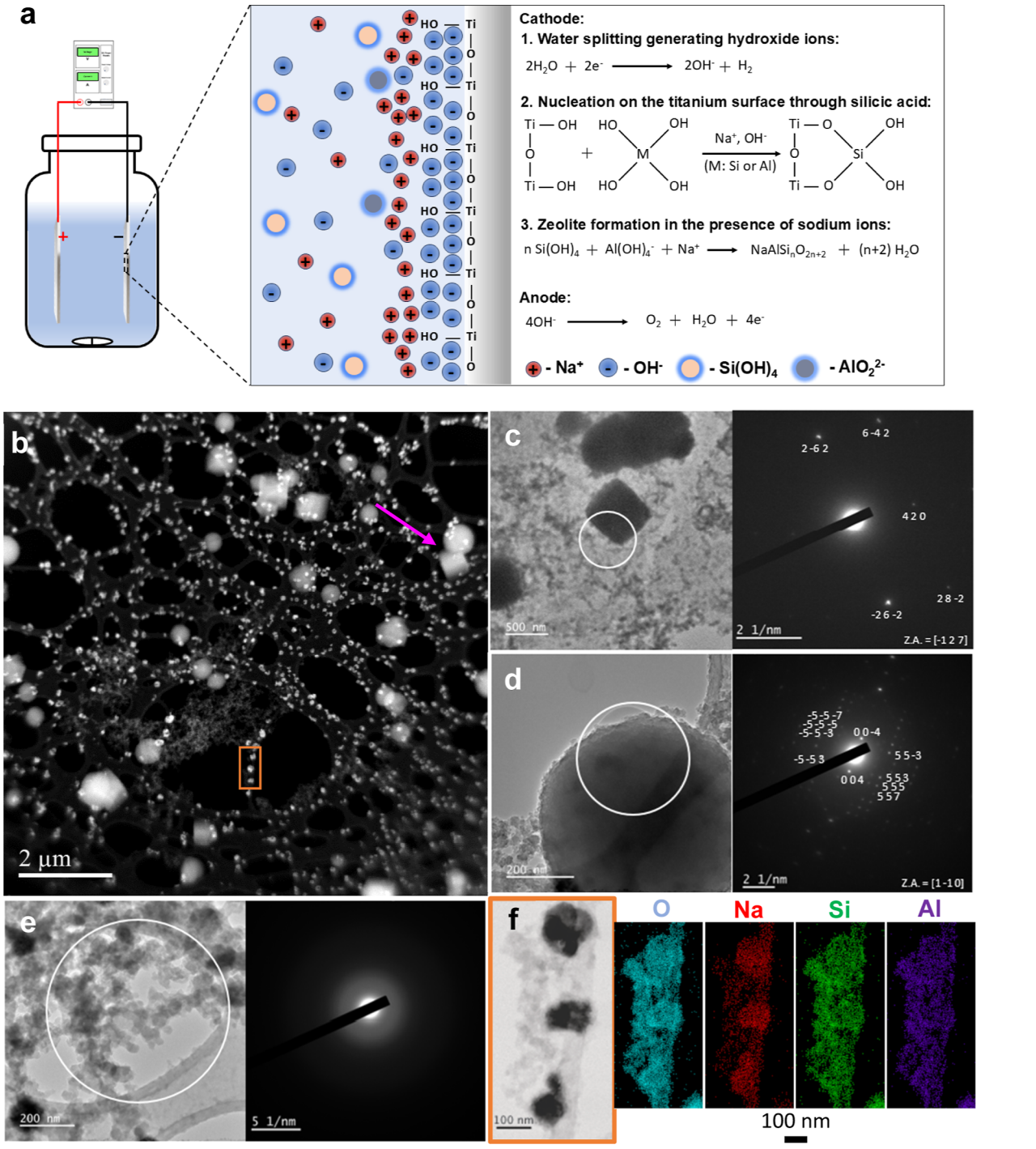

Figure 6. (a) Proposed electrochemical zeolite synthesis mechanism. (b) HAADF-STEM image of zeolite deposited on a gold grid in sampling experiment. The magenta arrow highlights two spherical and cubical zeolite particles fused together. TEM images and electron diffraction patterns of cubical LTA (c), spherical LTN (d), and amorphous aggregates in ribbon-like structure (e) in the deposited materials. (f) shows high magnification BF-STEM image of the region in (b) outlined by orange rectangle and corresponding EDS maps of the image indicating spatial distributions of O (cyan), Na (red), Si (green), and Al (purple) elements (synthesis conditions: Pt anode, Ti cathode, 1.00 A direct current, 363 K, ambient pressure, 200 rpm, 5 min deposition time).

cathode and the generation of hydroxide ions on the cathode electrode due to water electrolysis prompt the migration of positively charged template ions (e.g., Na^+). The high concentration of sodium ions near the cathode surface (Figure 6a) serves as structure-directing agents.

The exclusive growth of zeolite on the electrode surface (i.e., absence of nucleation and growth in the bulk phase) implies that heterogeneous nucleation and growth contribute to the electrochemical development of zeolite coatings. This should involve an interaction between the zeolite precursor species and the surface chemistry of the cathode. The alkaline solution and premixing should have hydrolyzed the colloidal silica and sodium aluminate precursors to form negatively charged silicate (SiO_4^{4-}) and aluminate (AlO_2^-) ions. However, direct

https://doi.org/10.1021/jacsau.4c00691
JACS Au 2024, 4, 4769−4779

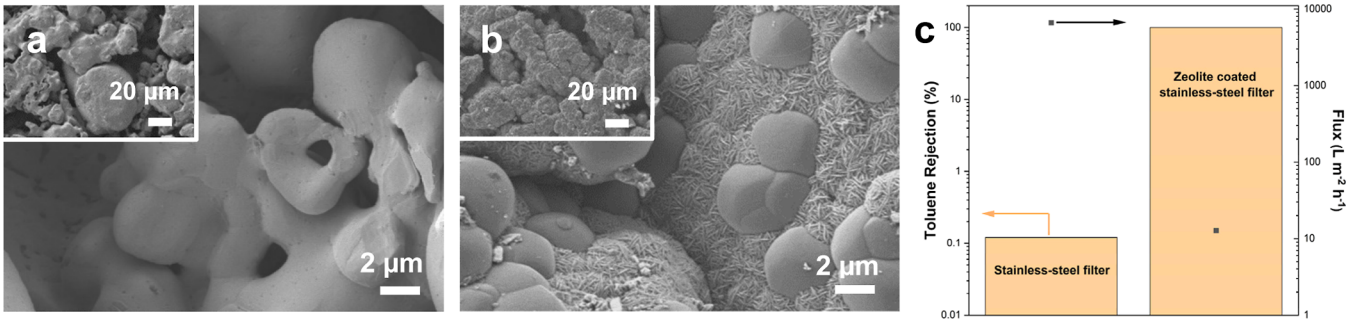

Figure 7. SEM images of the bare (a) and zeolite-coated (b) porous stainless-steel substrate. Insets in (a,b) show morphologies at lower magnification. (c) is the oil/water separation performance data obtained from materials in (a) and (b) (synthesis conditions for (b): Pt anode, porous stainless-steel cathode, 1.00 A direct current, 363 K, ambient pressure, 200 rpm stirring, 45 min deposition).

electrochemical deposition of these anions from the aqueous zeolite synthesis gel is not thermodynamically feasible due to the limited electrochemical window of water. According to the Pourbaix diagram,[50] Ti would be present as $HTiO_3^-$ in the zeolite synthesis gel composition (pH = 14.6), which coincides with the presence of enhanced oxygen signals in the titanium electrode observed in the EDS line scan (Figure 1e), suggesting the presence of Ti(OH) species on the cathode surface. Studies on zeolite crystallization diagrams[51] suggest that if the solution silicate ratio $[SiO_2]/[Na_2O]$ is less than 0.25 and Na/Al is higher than 4, monomeric (Q_1) and dimeric (Q_2) anions are present in significant amounts. It is reported that $Si(OH)_4$ condenses with any pre-existing solid surface that bears OH groups.[48] Therefore, we anticipate that titanium silicate forms accordingly (see eq 2 in Figure 6a).[48] Following titanium silicate formation, polymerization of anionic species would likely occur to enable heterogeneous nucleation. In addition, the presence of sodium ions, that serve as structure-directing agents, facilitates zeolite crystallization by shifting the reaction equilibrium to the right-hand side (as illustrated by eq 3 in Figure 6a), leading to growth of zeolite coatings (Figure 6a). A temperature gradient may exist within the interfacial layer between the cathode surface and the bulk electrolyte solution, potentially influencing the formation of zeolite coatings. However, due to the complexity of the reaction system, encompassing water splitting, Joule heating, overpotential effects, zeolite crystallization, etc., further investigation is required to confirm its specific impact.

To verify the proposed mechanism, the electrochemical synthesis of zeolite coatings was sampled by placing an amorphous carbon-coated gold transmission electron microscope grid on the cathode surface (see Section S1.4 in the Supporting Information file for details). After 5 min of electrochemical deposition, the gold grid was removed from the cathode surface and examined by high-angle annular dark-field scanning transmission electron microscopy (HAADF-STEM) and TEM. Notable features observed on the carbon film included ~0.5 μm cubic and spherical particles, rough ribbon-like films, and abundant ~0.1 μm particles (Figure 6b). Electron diffraction patterns of the ~0.5 μm cubic particles indicated a crystalline LTA phase (Figures 6c and S7a), while the ~0.5 μm spherical particles were identified as an LTN phase (Figures 6d and S7b). The ribbon-like film contained a network of small particles that were identified as amorphous (Figure 6e). The ~0.1 μm particles were found to be polycrystalline (Figure S8) and surrounded by an amorphous phase. STEM–EDX mapping revealed that the crystalline particles possessed cores rich in sodium compared to the particle exteriors and the surrounding amorphous phase (Figures 6f and S8c,d). The oxygen, silicon, and aluminum, however, were well distributed throughout the entire crystalline–amorphous body (Figures 6f and S8d).

The zeolite morphologies and phases in the TEM sampling experiment are consistent with those observed in the electrochemical deposition of zeolites at lower temperature (Figure 1b) or lower applied current (Figure 3a). The presence of an amorphous phase surrounding the crystalline core is consistent with previous observations of structural transformation from amorphous to crystalline in the stages of zeolite hydrothermal crystallization.[52] The appearance of Na-rich regions in the crystalline core is consistent with the proposed electrochemical zeolite coating formation mechanism in Figure 6a and with the sodium enrichment near the titanium electrode observed by SEM EDS (Figures 2b and S5). It is worth noting that even after only 5 min of electrochemical deposition, micrometer-sized crystalline LTA and LTN zeolites had already formed, suggesting expedited zeolite crystallization kinetics under the applied electrified field. In contrast, the growth of these zeolites takes significantly longer, ranging from several hours to a few days, under hydrothermal synthesis conditions, and as reported previously[37,53,54] and evidenced in our control experiment (Figure S10).

Electrochemically Deposited Zeolite Coatings for Separation and Pervaporation Applications

The electrochemical deposition of the zeolite coating is applicable to other metal substrates and more complicated geometries. Here, we employed a porous stainless-steel pellet (Figure 7a) as the cathode, on which the zeolite coating was developed using the same deposition conditions as those for Figure 4c. Similar to the morphology and crystalline phases observed on the flat titanium cathode, intertwined growth of cuboctahedron LTN and thread ball-like SOD zeolites was observed (Figure 7b). This zeolite coating significantly reduced the water contact angle (i.e., from ~99 to ~40.1°, Figure S11), indicating improved hydrophilicity of the metal substrate surface. This enhanced hydrophilicity was further leveraged to investigate the applicability of the zeolite-coated porous substrate for oil–water separations using a mixed toluene and water feed (50%/50% in volume, Figure 7c). The results demonstrated excellent separation performance compared with the bare stainless-steel support, with a toluene rejection of 99.5%. In contrast, the bare porous substrate exhibited a high flux with no rejection under the same test conditions.

https://doi.org/10.1021/jacsau.4c00691
JACS Au 2024, 4, 4769–4779

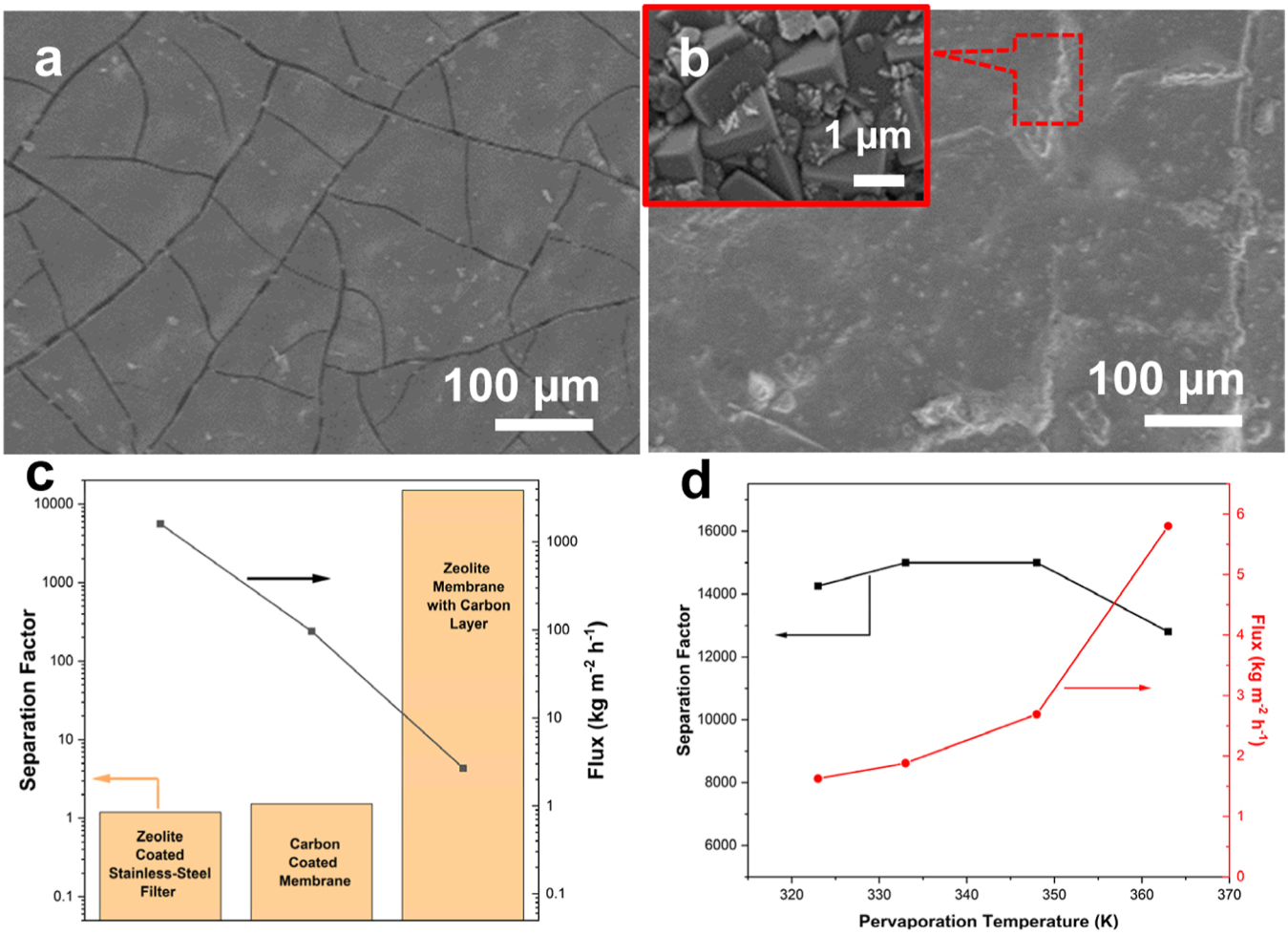

Figure 8. SEM images of carbon-coated (a) and zeolite coating on carbon-coated (b) porous stainless-steel substrate. Inset in (b) shows higher magnification of the LTA zeolite coating in the cracks. (c) is the ethanol/water pervaporation performance data obtained from materials in Figure 7b and 8a,b. (d) is the ethanol/water pervaporation performance at different temperatures (synthesis conditions for (b): Pt anode, carbon-coated porous stainless-steel cathode, 1.00 A direct current, 333 K, ambient pressure, 200 rpm stirring, 120 min deposition).

Zeolite membranes have been commercialized for pervaporation applications for dehydration of organic solvents. For example, the first large scale pervaporation plant based on the LTA zeolite was developed by Bussan Nanotech Research Institute Inc. (BNRI), Japan.[55] The membranes were developed on porous alumina/silica composite tubular supports using seed dip coating followed by hydrothermal treatment.[55] Other methods that utilized combined seeding methods involving rubbing and dip coating were developed which improved reproducibility and reduced synthesis times significantly.[56] Industrial-scale LTA zeolite membranes have been produced on tubular supports to large units with capacities for dehydration of 15,000−50,000 tons of solvent per year.[57] To demonstrate application potential of as-developed zeolite coatings in this work, the zeolite coating on a stainless-steel pellet (Figure 7b) developed in this work underwent testing for ethanol pervaporation, using an ethanol−water mixture (10 wt % water/90 wt % ethanol) as a feed. Results revealed a high permeation flux of 1603 kg m^{-2} h^{-1} (Figure 8c) but a low selectivity (α = 1.19). This outcome is due to defects within the zeolite membrane since large pores exist in the stainless-steel substrate (Figure 7a). To address this challenge, an intermediate carbon layer was introduced onto the stainless-steel substrate prior to the electrochemical deposition of zeolite. The carbon barrier layer was created by impregnating the stainless-steel substrate with a polymer/carbon nanotube slurry (polymer: P84-polyimide (18 wt %); carbon nanotube (1 wt %); solvent: 1-Methyl-2-pyrrolidinone (81 wt %)), followed by pyrolysis at 600 °C (see Section S1.6 for details). The resulting carbon layer (Figure 8a) covered the substrate uniformly, albeit with some cracks. Subsequent electrochemical growth of zeolite on the carbon-coated stainless-steel substrate revealed LTA zeolite formation, filling the valleys of these cracks (Figure 8b). Ethanol/water pervaporation tests indicated that the sole carbon layer reduced the flux and failed to achieve high selectivity (i.e., 96.4 kg m^{-2} h^{-1}, α = 1.5, Figure 8c). In contrast, membranes with zeolite coatings on the carbon-coated stainless-steel substrate significantly enhanced pervaporation performance, yielding high selectivity (α > 15000) with varying flux between 2.7 kg m^{-2} h^{-1}. Changing the pervaporation temperature showed an increase in the pervaporation flux as the temperature was increased (Figure 8d). A large change in the flux from 2.7 to 5.8 kg m^{-2} h^{-1} is observed when the temperature is increased from 348 to 363 K accompanied by a reduction in the separation factor from >15000 to 12800. Higher temperatures would result in reduced water adsorption along with increased diffusion hindering the selectivity of the

https://doi.org/10.1021/jacsau.4c00691
JACS Au 2024, 4, 4769−4779

membrane. This pervaporation performance is comparable to previously reported results under similar conditions, as outlined in Table S2. Further, reproducibility is a crucial criterion for a fabrication method. Two other membranes with the same fabrication method were prepared. Similar fluxes and separation factors (>10000) were observed for both membranes (Figure S12).

CONCLUSIONS

In summary, zeolite coatings were synthesized by using an electrochemical deposition method. By controlling applied current, deposition time, and temperature, zeolites with varying morphologies and crystalline phases were obtained. The crystal polymorphism influenced by increased current progresses from amorphous to crystalline and low- to high-density zeolite frameworks, similar to the effects observed with elevated temperature or prolonged synthesis time. The coating thickness, however, does not exhibit a clear dependence on the current, a phenomenon likely stemming from the increasing heterogeneity of the electric field. This heterogeneity promotes lateral growth, transitioning from areas of surface coverage to adjacent empty regions. This self-regulating behavior deviates from the Oswald ripening and results in zeolite coatings with consistent thickness across the substrate surface.

The mechanism of electrochemical deposition of zeolite coatings was proposed, which involves the formation of Ti(OH) species on the cathode, electrolysis of water to produce OH^- ions, enrichment of positively charged Na^+ ions, and subsequent heterogeneous nucleation and growth of zeolite. In situ sampling studies provided evidence for the supporting proposed mechanism and confirmed the accelerated zeolite crystallization kinetics under the applied electric field. Electrochemical deposition of zeolite coatings was extended to a porous stainless-steel substrate, enhancing surface hydrophilicity and demonstrating efficient oil/water separation. The electrochemical deposition selectively occurs in the crack regions of carbon-coated porous stainless-steel substrates, forming a composite membrane with high ethanol/water pervaporation performance. The work represents the first report of electrochemically controlled polymorphism in zeolite synthesis for developing coatings and can be applied broadly to diverse zeolite framework types for substrates with complex geometries.

ASSOCIATED CONTENT

Supporting Information

The Supporting Information is available free of charge at https://pubs.acs.org/doi/10.1021/jacsau.4c00691.

Detailed experimental procedure including schematics of experimental setup and materials characterizations (SEM, TEM, SAED, XRD, and contact angle measurements) (PDF)

AUTHOR INFORMATION

Corresponding Author

Dongxia Liu − *Department of Chemical and Biomolecular Engineering, University of Delaware, Newark, Delaware DE 19716, United States;* orcid.org/0000-0001-8712-2219; Phone: (+1) 302-831-6725; Email: liud@udel.edu

Authors

Akash Warty − *Department of Chemical and Biomolecular Engineering, University of Delaware, Newark, Delaware DE 19716, United States;* orcid.org/0009-0008-1372-2586

Amy Chen − *Department of Materials Science and Engineering, University of Maryland, College Park, Maryland 20742, United States; DEVCOM Army Research Laboratory, FCDD-RLA-GD, Adelphi, Maryland 20783, United States*

Dat T. Tran − *DEVCOM Army Research Laboratory, FCDD-RLA-GD, Adelphi, Maryland 20783, United States*

Harrison Kraus − *Department of Chemical and Biomolecular Engineering, University of Maryland, College Park, Maryland 20742, United States*

Taylor J. Woehl − *Department of Chemical and Biomolecular Engineering, University of Maryland, College Park, Maryland 20742, United States;* orcid.org/0000-0002-4000-8280

Complete contact information is available at: https://pubs.acs.org/10.1021/jacsau.4c00691

Author Contributions

CRediT: **Akash Warty** conceptualization, formal analysis, investigation, methodology, writing - original draft, writing - review & editing; **Amy Chen** formal analysis, writing - review & editing; **Taylor J. Woehl** formal analysis, writing - review & editing; **Dongxia Liu** conceptualization, formal analysis, funding acquisition, methodology, supervision, writing - original draft, writing - review & editing

Notes

The authors declare the following competing financial interest(s): We are in the process of filing a Provisional Patent Application for this work.

ACKNOWLEDGMENTS

The authors acknowledge the funding support from the National Science Foundation (NSF-PFI-MCA-2220588) and Department of Energy (DESC0023357). A portion of this work was sponsored by the U.S. Army Combat Capabilities Development Command - Army Research Laboratory and was accomplished under an ARL Cooperative Research and Development Agreement (CRADA 14-052-22). T.J.W. and A.C. acknowledge support from the Petroleum Research Fund (#61111-DNI10). This research used instruments in the Advanced Materials Characterization Lab and W. M. Keck Center for Advanced Microscopy and Microanalysis at the University of Delaware.

REFERENCES

(1) Huang, A.; Yang, W.; Liu, J. Synthesis and Pervaporation Properties of NaA Zeolite Membranes Prepared with Vacuum-Assisted Method. *Sep. Purif. Technol.* **2007**, *56* (2), 158−167.

(2) Li, Y.; Chen, H.; Liu, J.; Yang, W. Microwave Synthesis of LTA Zeolite Membranes without Seeding. *J. Membr. Sci.* **2006**, *277* (1−2), 230−239.

(3) van Niekerk, A.; Zah, J.; Breytenbach, J. C.; Krieg, H. M. Direct Crystallisation of a Hydroxy Sodalite Membrane without Seeding Using a Conventional Oven. *J. Membr. Sci.* **2007**, *300* (1−2), 156−164.

(4) Wang, Z.; Ge, Q.; Gao, J.; Shao, J.; Liu, C.; Yan, Y. High-Performance Zeolite Membranes on Inexpensive Large-Pore Supports: Highly Reproducible Synthesis Using a Seed Paste. *ChemSusChem* **2011**, *4* (11), 1570−1573.

(5) Lai, Z.; Bonilla, G.; Diaz, I.; Nery, J. G.; Sujaoti, K.; Amat, M. A.; Kokkoli, E.; Terasaki, O.; Thompson, R. W.; Tsapatsis, M.; Vlachos, D. G. Microstructural Optimization of a Zeolite Membrane for Organic Vapor Separation. *Science* **2003**, *300* (5618), 456−460.
(6) Varoon Agrawal, K.; Zhang, X.; Elyassi, B.; Brewer, D. D.; Gettel, M.; Kumar, S.; Lee, J. A.; Maheshwari, S.; Mittal, A.; Sung, C. Y.; Cococcioni, M.; Francis, L. F.; McCormick, A. V.; Mkhoyan, K. A.; Tsapatsis, M. Dispersible Exfoliated Zeolite Nanosheets and Their Application as a Selective Membrane. *Science* **2011**, *334* (6052), 72−75.
(7) Dakhchoune, M.; Villalobos, L. F.; Semino, R.; Liu, L.; Rezaei, M.; Schouwink, P.; Avalos, C. E.; Baade, P.; Wood, V.; Han, Y.; Ceriotti, M.; Agrawal, K. V. Gas-Sieving Zeolitic Membranes Fabricated by Condensation of Precursor Nanosheets. *Nat. Mater.* **2021**, *20* (3), 362−369.
(8) Wang, X.; Tan, X.; Meng, B.; Zhang, X.; Liang, Q.; Pan, H.; Liu, S. TS-1 zeolite as an effective diffusion barrier for highly stable Pd membrane supported on macroporous α-Al2O3 tube. *RSC Adv.* **2013**, *3* (14), 4821−4834.
(9) Pati, S.; Dewangan, N.; Wang, Z.; Jangam, A.; Kawi, S. Nanoporous Zeolite-A Sheltered Pd-Hollow Fiber Catalytic Membrane Reactor for Propane Dehydrogenation. *ACS Appl. Nano Mater.* **2020**, *3* (7), 6675−6683.
(10) Li, H.; Qiu, C.; Ren, S.; Dong, Q.; Zhang, S.; Zhou, F.; Liang, X.; Wang, J.; Li, S.; Yu, M. Na+-Gated Water-Conducting Nanochannels for Boosting CO2 Conversion to Liquid Fuels. *Science* **2020**, *367* (6478), 667−671.
(11) Yue, W.; Li, Y.; Wei, W.; Jiang, J.; Caro, J.; Huang, A. Highly Selective CO2 Conversion to Methanol in a Bifunctional Zeolite Catalytic Membrane Reactor. *Angew. Chem., Int. Ed.* **2021**, *60* (33), 18289−18294.
(12) Kim, S. J.; Liu, Y.; Moore, J. S.; Dixit, R. S.; Pendergast, J. G.; Sholl, D.; Jones, C. W.; Nair, S. Thin Hydrogen-Selective SAPO-34 Zeolite Membranes for Enhanced Conversion and Selectivity in Propane Dehydrogenation Membrane Reactors. *Chem. Mater.* **2016**, *28* (12), 4397−4402.
(13) Wang, Z.; Xu, J.; Pati, S.; Chen, T.; Deng, Y.; Dewangan, N.; Meng, L.; Lin, J. Y. S.; Kawi, S. High H_2 Permeable SAPO-34 Hollow Fiber Membrane for High Temperature Propane Dehydrogenation Application. *AIChE J.* **2020**, *66* (9), No. e16278.
(14) Min, B.; Korde, A.; Yang, S.; Kim, Y.; Jones, C. W.; Nair, S. Separation of 2 hydrocarbons from methane by zeolite MFI hollow fiber membranes fabricated from 2D nanosheets. *AIChE J.* **2021**, *67* (1), No. e17048.
(15) Kurzweil, P.; Maunz, W.; Plog, C. Impedance of Zeolite-Based Gas Sensors. *Sens. Actuators, B* **1995**, *25* (1−3), 653−656.
(16) Zhou, J.; Li, P.; Zhang, S.; Long, Y.; Zhou, F.; Huang, Y.; Yang, P.; Bao, M. Zeolite-Modified Microcantilever Gas Sensor for Indoor Air Quality Control. *Sens. Actuators, B* **2003**, *94* (3), 337−342.
(17) Huang, H.; Zhou, J.; Chen, S.; Zeng, L.; Huang, Y. A Highly Sensitive QCM Sensor Coated with Ag+-ZSM-5 Film for Medical Diagnosis. *Sens. Actuators, B* **2004**, *101* (3), 316−321.
(18) Mintova, S.; Mo, S.; Bein, T. Humidity Sensing with Ultrathin LTA-Type Molecular Sieve Films Grown on Piezoelectric Devices. *Chem. Mater.* **2001**, *13* (3), 901−905.
(19) Cai, R.; Sun, M.; Chen, Z.; Munoz, R.; Oneill, C.; Beving, D. E.; Yan, Y. Ionothermal Synthesis of Oriented Zeolite AEL Films and Their Application as Corrosion-Resistant Coatings. *Angew. Chem., Int. Ed.* **2008**, *47* (3), 525−528.
(20) Lew, C. M.; Cai, R.; Yan, Y. Zeolite Thin Films: From Computer Chips to Space Stations. *Acc. Chem. Res.* **2010**, *43* (2), 210−219.
(21) Ferreira, L.; Fonseca, A. M.; Botelho, G.; Aguiar, C. A.; Neves, I. C. Antimicrobial Activity of Faujasite Zeolites Doped with Silver. *Microporous Mesoporous Mater.* **2012**, *160*, 126−132.
(22) Kwakye-Awuah, B.; Williams, C.; Kenward, M. A.; Radecka, I. Antimicrobial Action and Efficiency of Silver-Loaded Zeolite X. *J. Appl. Microbiol.* **2008**, *104* (5), 1516−1524.
(23) Rivera-Garza, M.; Olguín, M. T.; García-Sosa, I.; Alcántara, D.; Rodríguez-Fuentes, G. Silver Supported on Natural Mexican Zeolite as an Antibacterial Material. *Microporous Mesoporous Mater.* **2000**, *39* (3), 431−444.
(24) Calabrese, L. Anticorrosion Behavior of Zeolite Coatings Obtained by In Situ Crystallization: A Critical Review. *Materials* **2018**, *12* (1), 59.
(25) Li, H.; Xu, J.; Wang, J.; Yang, J.; Bai, K.; Lu, J.; Zhang, Y.; Yin, D. Seed-Free Synthesis of Highly Permeable Zeolite NaA Membranes through Deposition of APTES-Functionalized Alumina Particles on Macroporous Supports. *J. Membr. Sci.* **2014**, *471*, 84−93.
(26) Rao, P. R. H. P.; Matsukata, M. Dry-Gel Conversion Technique for Synthesis of Zeolite BEA. *Chem. Commun.* **1996**, *12*, 1441−1442.
(27) Cai, R.; Liu, Y.; Gu, S.; Yan, Y. Ambient Pressure Dry-Gel Conversion Method for Zeolite MFI Synthesis Using Ionic Liquid and Microwave Heating. *J. Am. Chem. Soc.* **2010**, *132* (37), 12776−12777.
(28) Simon, U.; Flesch, U.; Maunz, W.; Müller, R.; Plog, C. The Effect of NH3 on the Ionic Conductivity of Dehydrated Zeolites Na Beta and H Beta. *Microporous Mesoporous Mater.* **1998**, *21* (1−3), 111−116.
(29) Kelemen, G.; Schön, G. Ionic Conductivity in Dehydrated Zeolites. *J. Mater. Sci.* **1992**, *27* (22), 6036−6040.
(30) Cundy, C. S.; Cox, P. A. The Hydrothermal Synthesis of Zeolites: Precursors, Intermediates and Reaction Mechanism. *Microporous Mesoporous Mater.* **2005**, *82* (1−2), 1−78.
(31) Elnekave, M.; Tatlier, M. Electrochemical Properties of Gel-Type Zeolite Synthesis Mixtures. *Chem. Eng. Commun.* **2008**, *195* (6), 661−673.
(32) Huang, A.; Liu, D.; Li, Y.; Lin, Y.; Yang, W. Preparation of A-Type Zeolite Membranes on Nonporous Metal Supports by Using Electrophoretic Technique. *Chin. Sci. Bull.* **2004**, *49* (12), 1226−1230.
(33) Huang, A.; Yang, W. Hydrothermal Synthesis of Uniform and Dense NaA Zeolite Membrane in the Electric Field. *Microporous Mesoporous Mater.* **2007**, *102* (1−3), 58−69.
(34) Yu, T.; Chu, W.; Cai, R.; Liu, Y.; Yang, W. In Situ Electrochemical Synthesis of Oriented and Defect-Free AEL Molecular-Sieve Films Using Ionic Liquids. *Angew. Chem., Int. Ed.* **2015**, *54* (44), 13032−13035.
(35) Ivanushkin, G.; Dusselier, M. Engineering Lewis Acidity in Zeolite Catalysts by Electrochemical Release of Heteroatoms during Synthesis. *Chem. Mater.* **2023**, *35* (13), 5049−5058.
(36) Ivanushkin, G.; Torka Beydokhti, M.; Martinez-Espin, J. S.; Dusselier, M. Electro-Assisted Synthesis of Sn-Beta Zeolite Leads to Record Tin Incorporation and Superior Lewis Acid Catalysis. *Chem. Mater.* **2023**, *35* (23), 10216−10227.
(37) Maldonado, M.; Oleksiak, M. D.; Chinta, S.; Rimer, J. D. Controlling Crystal Polymorphism in Organic-Free Synthesis of Na-Zeolites. *J. Am. Chem. Soc.* **2013**, *135* (7), 2641−2652.
(38) Greer, H.; Wheatley, P. S.; Ashbrook, S. E.; Morris, R. E.; Zhou, W. Early Stage Reversed Crystal Growth of Zeolite A and Its Phase Transformation to Sodalite. *J. Am. Chem. Soc.* **2009**, *131* (49), 17986−17992.
(39) Peng, H.; Ding, M.; Vaughan, J. The Anion Effect on Zeolite Linde Type A to Sodalite Phase Transformation. *Ind. Eng. Chem. Res.* **2018**, *57* (31), 10292−10302.
(40) Subotić, B.; Škrtić, D.; Šmit, I.; Sekovanić, L. Transformation of Zeolite A into Hydroxysodalite: I. An Approach to the Mechanism of Transformation and Its Experimental Evaluation. *J. Cryst. Growth* **1980**, *50* (2), 498−508.
(41) Subotić, B.; Sekovanić, L. Transformation of Zeolite A into Hydroxysodalite: II. Growth Kinetics of Hydroxysodalite Microcrystals. *J. Cryst. Growth* **1986**, *75* (3), 561−572.
(42) Auerbach, S. M.; Ford, M. H.; Monson, P. A. New Insights into Zeolite Formation from Molecular Modeling. *Curr. Opin. Colloid Interface Sci.* **2005**, *10* (5−6), 220−225.
(43) Ahlers, C. B.; Talbot, J. B. Fabrication of Zeolite-Modified Electrodes via Electrophoretic Deposition. *J. Electrochem. Soc.* **1999**, *146* (9), 3259−3263.

https://doi.org/10.1021/jacsau.4c00691
JACS Au 2024, 4, 4769−4779

(44) Mittal, M.; Lobo, R. F.; Furst, E. M. Externally Directed Assembly of Disk-Shaped Zeolite Particles by an Electric Field. *J. Mater. Res.* **2011**, *26*, 215−222.
(45) Liu, D.; Savino, K.; Yates, M. Z. Microstructural Engineering of Hydroxyapatite Membranes to Enhance Proton Conductivity. *Adv. Funct. Mater.* **2009**, *19* (24), 3941−3947.
(46) Liu, D.; Savino, K.; Yates, M. Z. Coating of Hydroxyapatite Films on Metal Substrates by Seeded Hydrothermal Deposition. *Surf. Coat. Technol.* **2011**, *205* (16), 3975−3986.
(47) Oh, S. C.; Xu, J.; Tran, D. T.; Liu, B.; Liu, D. Effects of Controlled Crystalline Surface of Hydroxyapatite on Methane Oxidation Reactions. *ACS Catal.* **2018**, *8* (5), 4493−4507.
(48) Veeraraghavan, B.; Haran, B.; Slavkov, D.; Prabhu, S.; Popov, B.; Heimann, B. Development of a Novel Electrochemical Method to Deposit High Corrosion Resistant Silicate Layers on Metal Substrates. *Electrochem. Solid-State Lett.* **2003**, *6* (2), B4.
(49) Lechert, H. The PH Value and Its Importance for the Crystallization of Zeolites. *Microporous Mesoporous Mater.* **1998**, *22* (4−6), 519−523.
(50) Pourbaix, M. J. *Atlas of Electrochemical Equilibria in Aqueous Solutions*, 2nd English ed. ed.; National Association of Corrosion Engineers, 1974.
(51) Šefčík, J.; McCormick, A. V. Prediction of Crystallization Diagrams for Synthesis of Zeolites. *Chem. Eng. Sci.* **1999**, *54* (15−16), 3513−3519.
(52) Smaihi, M.; Barida, O.; Valtchev, V. Investigation of the Crystallization Stages of LTA-Type Zeolite by Complementary Characterization Techniques. *Eur. J. Inorg. Chem.* **2003**, *2003* (24), 4370−4377.
(53) Oleksiak, M. D.; Rimer, J. D. Synthesis of Zeolites in the Absence of Organic Structure-Directing Agents: Factors Governing Crystal Selection and Polymorphism. *Rev. Chem. Eng.* **2014**, *30* (1), 1−49.
(54) Wenqin, P.; Ueda, S.; Koizumi, M. The Synthesis of Zeolite NaA from Homogeneous Solutions and Studies of Its Properties. *Stud. Surf. Sci. Catal.* **1986**, *28*, 177−184.
(55) Morigami, Y.; Kondo, M.; Abe, J.; Kita, H.; Okamoto, K. The First Large-Scale Pervaporation Plant Using Tubular-Type Module with Zeolite NaA Membrane. *Sep. Purif. Technol.* **2001**, *25* (1−3), 251−260.
(56) Liu, Y.; Yang, Z.; Yu, C.; Gu, X.; Xu, N. Effect of Seeding Methods on Growth of NaA Zeolite Membranes. *Microporous Mesoporous Mater.* **2011**, *143* (2−3), 348−356.
(57) Rangnekar, N.; Mittal, N.; Elyassi, B.; Caro, J.; Tsapatsis, M. Zeolite Membranes − a Review and Comparison with MOFs. *Chem. Soc. Rev.* **2015**, *44* (20), 7128−7154.

https://doi.org/10.1021/jacsau.4c00691
JACS Au 2024, 4, 4769−4779